# MOTESS-GNAT Sky Survey: MG1 Long Period Variable Stars Re-Visited After 10 Years

**Brian L. Craine**
*Western Research Company, Inc. and GNAT, Inc., 3275 W. Ina Road, Suite 221-A1, Tucson, AZ 85741; send email correspondence to blcraine@wrc-inc.com*

**Andrew S. Kulessa**
*Colin Gum Observatory, Greenhill, SA, Australia; GNAT, Inc., 3275 W. Ina Road, Suite 221-A1, Tucson, AZ 85745; andskul@gmail.com*

**Eric R. Craine**
*Western Research Company, Inc. and GNAT, Inc., 3275 W. Ina Road, Suite 221-A1, Tucson, AZ 85741; ercraine@wrc-inc.com*

**Roger B. Culver**
*GNAT, Inc., 3275 W. Ina Road, Suite 221-A1, Tucson, AZ 85741; Professor Emeritus of Astronomy, Colorado State University, Fort Collins, CO 80523; Roger.Culver@coloradostate.edu*

**Adam L. Kraus**
*Department of Astronomy, University of Texas, Austin, TX 78712; alk@astro.as.utexas.edu*

**Roy A. Tucker**
*Tucson, AZ (deceased)*

**Douglas K. Walker**
*Prime Solutions Group, Inc and GNAT, Inc., 3275 W. Ina Road, Suite 221-A1, Tucson, AZ 85741; dougwalker@psg-inc.net*

*Received August 9, 2022; revised November 25, 2022; accepted December 6, 2022*

**Abstract** The MG6 survey is a 10-year follow-up to the MG1 survey. A new reduction of these surveys has been performed and screened for candidate long period variable stars (LPVs). In combination with the original 47 LPVs found in the MG1 variable star candidate catalog a total of 138 LPVs have been identified in the MG1 48.3'-wide equatorial strip. The additional data have allowed for refinement of the period determinations for most of the LPVs. Some of the biases of the selected population with respect to period length and color distribution are examined. This study has newly identified 9 unique LPVs, bringing the total number of new LPV identifications from the MOTESS-GNAT survey to 56. The number of LPVs in this list exhibiting hump characteristics has been expanded to at least 15.

## 1. Introduction

Since 2001 the Moving Object and Transient Event Search System (MOTESS) (Tucker 2007) and the Global Network of Astronomical Telescopes (GNAT) have collaborated to produce equatorial sky surveys and data reduction pipelines useful for the discovery and characterization of variable stars. The first MG1 data pipeline (Kraus *et al.* 2007) produced a subset of candidate variable stars numbering about 26,000 out of the nearly two million stars detected. This work is referred to as the "MG1 Variable Star Catalog" (MG1-VSC).

Among the variable stars characterized are the long period variables (LPVs) detected in MG1-VSC (Craine *et al.*, 2015). Since publication of those observations a second survey (MG6) has been completed; this survey was conducted for the same survey strip that was observed for MG1 but 10 years later, hence adding additional temporally distributed observations of this set of LPVs. Further, the MG1 observations have been re-reduced using a newly developed pipeline which generates a comprehensive database of light curves of all the stars detected in the survey images (Craine *et al.* 2021). The MG6 survey data have been reduced using the same protocols.

Reported here are the results of the additional observations of LPVs resulting from re-evaluation of the MG1 and MG6 databases.

## 2. Methods

The MG1 and MG6 survey images (section 2.1) were reduced to produce the MG1A and MG6A databases of unsaturated objects and associated screening parameters (section 2.2). Some of those parameters were used as selection criteria for potential LPVs (section 2.3). The original images containing the potential LPVs were then subjected to more stringent photometry (section 2.4) and these data were used to determine an estimate of the period (section 2.5). This section provides more detail on these steps and other methodology.

2.1. Observations

The MG1 and MG6 surveys consisted of scan mode images centered at a declination of +03° 18' 20" with a width of 48.3' in declination obtained between 2001–2003 (282 nights observing) and 2011–2013 (232 nights observing), respectively, with each object typically observed three times per night at 20-minute intervals by the MOTESS system (Tucker 2007; Kraus *et al.* 2007). The image scale for the scan mode images was 2.83 arcsec/pixel. Unfiltered observations with an integration time of 192 seconds yielded a practical detection range of 12.6 to 17.4 in Gaia R band magnitude.

2.2. Data reduction

The MG1 and MG6 survey images were processed, analyzed, and the data organized into SQL databases for each survey using dedicated Python scripts that relied upon the Astropy library as described (Craine *et al.* 2021). These databases were designated MG1A and MG6A. The light curve data saved to the MG1A and MG6A databases were obtained using an unsupervised pipeline that employed a high image stringency that rejected many images that contained usable data for some objects in the image. In addition, the data were obtained from only two of the three telescopes (A and B) in the MOTESS system (Tucker 2007). Single aperture photometry with an ensemble comparison was used to determine the screening light curves (see Craine *et al.* 2021 for details).

Parameters calculated for each object included the Lomb-Scargle false alarm probability (FAP) (Press 1996; Scargle 1982), the inverse of the Von Neuman ratio (1/η) index (Von Neumann 1941), Equation (1), and the short-term slope (μ), Equation (2).

The inverse Von Neuman index is calculated as:

$$1/\eta = \frac{(N-1)\,\sigma^2}{\sum_{i=1}^{N-1}(m_{i+1}-m_i)^2}, \qquad (1)$$

where N is the number of observations, m is the magnitude of the observations in order of observation time, and σ is the standard deviation of the magnitudes. The Von Neuman statistic, η, is the mean square successive difference of the time series divided by the sample variance, which is small when there is strong positive serial correlation between successive data points. This is a statistical test for the serial dependence of a time series of data (i.e., $H_0$:; there is no serial correlation of successive magnitudes). The inverse Von Neuman index is a convenient metric which increases in value for variable objects. The observed range of 1/η for survey objects was 0.27 to 21.9.

A new metric specifically tailored for the detection of long period variables, the short-term slope (μ), is introduced. This metric calculates the average absolute value of the slope of sub-intervals of a light curve. It is calculated as:

$$\mu = \frac{\sum_{n=1}^{n=\left|\frac{\Delta t}{\delta}\right|}\left|\frac{\sum_{i=1}^{kn}(t_i-\bar{t})(m_i-\bar{m})}{\sum_{i=1}^{k_n}(t_i-\bar{t})^2}\right|}{\left|\frac{\Delta t}{\delta}\right|}, \qquad (2)$$

where $t_i$ is the time of ith observation in the nth interval, $m_i$ is the differential magnitude at $t_i$, t-bar is the average time of observations in the nth interval, m-bar is the average magnitude of observations in the nth interval, Δt is the total time of the survey, δ is a selected time sub-interval (which was 60 days for the LPV search), and $k_n$ is the number of observations in the nth interval. This parameter is sensitive to increasing or decreasing trends in magnitude over times scales of multiples of δ. For convenience the μ metric was scaled to a slope per ~5.184 days ($10^6$ seconds). The theoretical range of μ is 0 to undefined. In practice, the survey objects had an observed range of 0.0 to 3.2.

2.3. LPV selection

The selection of the potential LPV objects was a two-step procedure. First, objects in the databases were selected by the union of objects with an FAP < 0.00001, μ > 0.09, and 1/η >5.0. These cutoffs were selected as values that maximized the enrichment of LPVs in the selected objects. This enrichment averaged about $10^4$-fold (detailed in section 3.1, Table 1). Secondly, the light curves from these objects were screened visually and obvious erroneous assignments, typically due to outlier points from a small number of bad images that survived initial quality checks, were rejected.

2.4. Photometry

To provide a more robust data set, selected potential LPV objects were re-analyzed employing the annular photometry routine from Astropy (Astropy Collab. 2018, ; Bradley *et al.*, 2019). All images containing the object, including those from the third telescope, were measured. This made maximum use of images available for each LPV candidate. Two nearby reference and check stars (typically within a 5' radius) were selected for least crowded backgrounds. Since the images are obtained in scan mode the reference and check stars may unpredictably fall out of some frames. Consequently, the combination of reference and check stars producing the greatest number of measurements was finally used. The aperture radius was 4px and the annulus had an inner radius of 6px and an outer radius of 10px for all objects. The target measurements were rejected when the corresponding check star magnitude exceeded ±2 standard deviations of the average for the check star. These are the light curves described below (see Appendix B).

2.5. Period determination

The light curves from the annular photometry were analyzed to determine a period for the objects using a Generalized Lomb-Scargle periodogram (GLS) algorithm (Zechmeister and Kürster 2009; VanderPlas 2018).

The GLS algorithm solves for the coefficients Aω, Bω, and Cω in a model describing magnitude as a function of time (M(t)), given by equation (3):

$$M(t) = A\omega \sin(\omega t) + B\omega \cos(\omega t) + C\omega, \qquad (3)$$

by least squares over a frequency grid, ω. The frequency corresponding to the maximum in the periodogram is chosen as the optimum frequency and the corresponding coefficients define the light curve model. Often there can be ambiguity

Table 1. Results of screening MG1 and MG6 for LPVs.

| *Database* | *Pre-Screen* | *Post-Screen* | *Visual Accepted* |
|---|---|---|---|
| MG1A | 936,764 | 73 | 43 |
| MG6A | 1,046,732 | 111 | 95 |

between periodogram peaks and in these cases a method based on statistical inference employing the Vuong statistic as outlined in (Baluev 2012) is used to distinguish the preferred light curve model.

The Vuong statistic is computed for pairs of rival models, corresponding to peaks in the periodogram. This statistic tests the null hypothesis that the difference between models is consistent with random noise, while applying a significance level of 0.05.

Aliasing was resolved by inspection of time series light curves (when available) from higher cadence observations from the Zwicky Transient Facility (Bellm *et al.* 2019) or ASAS-SN observations (Kochanek *et al.* 2017; Shappee *et al.* 2014).

The GLS algorithm was implemented in the Python class Gls.py (Zechmeister 2019) for all LPV candidates. A large subset of the data was also analyzed using GNAT software developed by one of the authors (A. Kulessa). Period determinations between the two codes agreed to within one day. The amplitude of objects was determined from the best light curve model according to Equation (4). This approach allows for the amplitude determination even in the case where the maximum or minimum is not observed.

$$\text{full amplitude} = 2\left(\sqrt{(A_\omega^2 + B_\omega^2)}\right), \quad (4)$$

2.6. LPV hump measurement

LPV hump structure was identified by visual examination of light curves. A fourth order polynomial fit to the data points surrounding the hump was determined, as illustrated in Figure 1A. This section of the light curve was detrended using the determined fit yielding the recognizable hump structure as in Figure 1B. The magnitude of the hump, Δm, is measured as the magnitude at the peak time. The duration is measured as the time from the rise to the fall of the curve from 0. The phase position of the hump is calculated from the peak time and the determined period and zero time for the LPV.

2.7. Statistics

Distributions were tested for similarity using the nonparametric Kolmogorov–Smirnov two-sample test $H_0$:; the two populations from which our samples were drawn have the same distribution function, critical p-value of 0.05). The difference between sample means was tested with the two-sample t-test ($H_0$: sample means are the same, critical p-value of 0.05). Calculations were performed using the Python scipy.stats library (Virtanen *et al.* 2020).

## 3. Results

3.1. Screening for LPVs

The completion of the MG6A database and the MG1A database together with the original MG1-VSC provides three

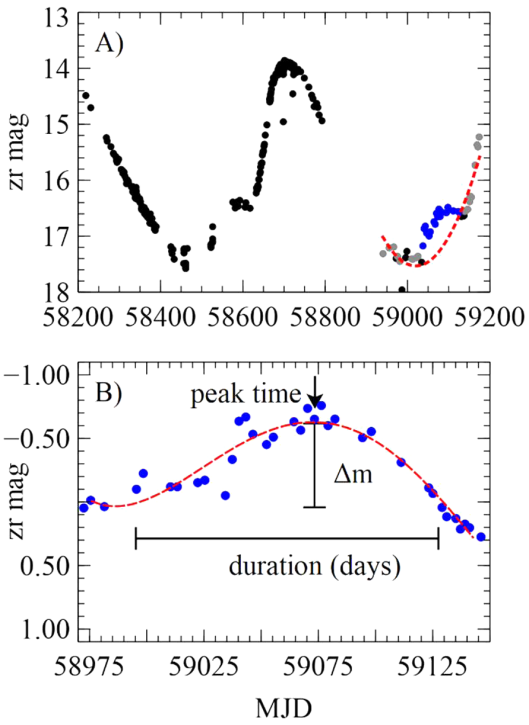


Figure 1. Measuring an LPV hump. (A) is the light curve for a LPV with an identified hump marked as blue dots and the nearby surrounding points marked as gray dots. The red dashed line is a polynomial fit to the surrounding gray dots. (B) is the detrended hump points as blue dots obtained by subtracting the fitted line from panel A from the light curve. The red dashed line is a polynomial fit to the hump.

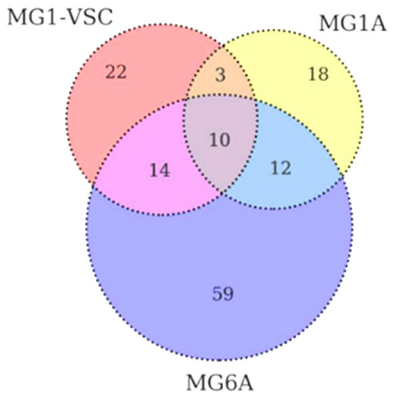


Figure 2. Venn diagram showing the distribution of LPV candidates identified by the three different surveys of a 48' declination strip centered at +03° 18′ 20″.

different approaches to recover LPVs from the +03° 18' 20" survey strip. The primary differences in the surveys are the data reduction methods (MG1A and MG6A versus MG1-VSC) or survey epoch (MG1-VSC and MG1A versus MG6A). These differences manifested in identification of overlapping and unique LPVs between the surveys as summarized in the Venn diagram shown in Figure 2.

The LPV candidates were selected from the MG1A and MG6A databases by applying cutoff values for three key parameters—Lomb-Scargle false alarm probability, inverse Von Neuman index, and the short-term slope value—to the entire collection of detected survey objects. This resulted in a small number of objects highly enriched for LPVs (see Table 1).

The post-screen objects were then manually examined for final verification as an LPV.

The MG1-VSC identified variable stars using the Welch-Stetson index (Welch and Stetson 1993) to create a database of 26,042 variable star candidates. The light curves of objects from this database were manually searched multiple times by at least two separate investigators, resulting in the discovery of 47 LPV candidate stars (Craine *et al.* 2007).

Each of the three surveys provides a unique, but related, window on the identification of LPV candidates. These relationships can be viewed in more detail in the Venn diagram shown in Figure 2. As expected, many of the objects are observed in more than one survey. Each survey also has uniquely detected objects. MG1A and MG6A, which share methodology, have 22 candidates in common, while MG1-VSC and MG1A, which share epochs, have 13 candidates in common. MG1-VSC and MG6A, which only share the same declination strip, have 24 candidates in common. A total of 138 candidates were found. The diagram graphically shows the large contribution that the MG6 survey has added to the discovery of LPV candidates, suggesting that the key survey parameter is not the data processing methodology but factors affecting the image collection.

### 3.2. Characterization of LPV candidates

#### 3.2.1. Observed periods

The screened objects were selected, in part, for having a high probability of being periodic based upon a Lomb-Scargle analysis (Press 1996; Scargle 1982). However, the period obtained during screening is not a reliable period due to aliasing, sampling cadences, and sample size. Therefore, the LPV candidates were re-examined using all the survey images, which included images from all three telescopes of the MOTESS system. The photometry was performed using a local background estimation by the annular photometry method with two check stars and two comparison stars. This allowed for the recovery of usable data that had been discarded in a conservative unsupervised manner in the original screen. The enlarged pool of measurements was then smoothed with a five-day recursive median filter for period analysis.

The period was determined as described in the methods (section 2.5). The distribution of periods for the candidates is shown in Figure 3. LPVs are often characterized as having periods between 80 and 1,000 days (Percy 2007). The observed distribution from the MG survey is not normally distributed and is primarily in the 200–400-day range with an apparent under-representation of longer periods. This relatively narrow distribution could result from the actual range of LPV periods or a consequence of the inherent observing cadence of the survey. The black-dotted line in Figure 3 is the distribution fit to the periods for LPVs in the GaiaDR2 survey (Mowlavi 2018), which is different from the MG period distribution (Kolmogorov-Smirnov statistic = 0.31, $P < 1.4 \times 10^{-5}$). The mean periods of the MG data are different from the mean of the GaiaDR2 (275 d versus 341 d, respectively, $P_{(same)} < 1.4 \times 10^{-7}$), supporting the conclusion that the MG survey may be under-represented in longer period variables due to systematic limitations. The distribution of LPVs (Miras) from the ASAS-SN sky survey (Kochanek *et al.* 2017; Shappee *et al.* 2014) was not significantly different from the MG survey (P = 0.147) and the mean periods (275 d versus 288 d, $P_{(same)} = 0.174$) were not significantly different.

The Gaia DR2 survey (Mowlavi 2018) LPVs included 55 of the MG candidates and a comparison of the periods determined between the two surveys is presented in Figure 4. The agreement is quite good despite the lack of overlap in the actual timing of the surveys. LPVs are known to change their periods over time, and this may account for the small number of stars showing greater divergence from the expected value and may be good candidates for the study of more rapidly evolving stars. One of the divergent periods appears consistent with being a harmonic error in Gaia period determination (MG6A 10639637).

A similar comparison with 24 MG candidates overlapping with GCVS catalog (Samus *et al.* 2017) LPVs revealed a particularly good agreement for 20 of the stars (see Figure 5). Two of the stars (MG1 1388633 and MG6A 10854654) appeared to be significantly different. Despite being suspicious multiples of the GCVS period, a review of the MG data did not justify a period change.

The periods determined for the enlarged dataset, MG1A and MG6A, were also compared with the periods initially published using only the data from the original MG1-VSC (Craine *et al.* 2015). The results confirmed earlier expressed concerns about data aliasing in the MG survey data with significant changes in period assignment for 6 of the LPVs (see Figure 6).

#### 3.2.2. Color relationship

The LPV stars are red giants occupying a characteristic position on the Hertzsprung–Russell diagram. Ninety-three of the MG candidates could be found in the Gaia DR2 source database, providing the absolute G, B, and R band magnitudes allowing for the evaluation of the color characteristics for 82 of them. Figure 7 shows their placement on a Color Absolute Magnitude Diagram (CMD) and comparison with the characteristics of the LPVs identified by the Gaia DR2 survey (Mowlavi 2018). The MG candidates that could be evaluated appear as might be expected for a collection of LPV stars except for three to four objects that were not as red as might be expected.

Closer inspection of the CMD suggests that the MG candidates are more concentrated in the redder region of the diagram than the average LPV. This is verified in Figure 8, which shows a detailed comparison of the distribution of MG candidates and the larger collection of Gaia DR2 LPVs. The color distributions are significantly different ($P < 0.00001$, KS two-sample test) with the average MG candidate having a B–R of about 5.2 compared to the Gaia DR2 collection of about 3.0 (significance $p < 0.00001$, t-test for equal means). Comparing the MG survey to the ASAS-SN survey also shows a significantly different color distribution (P = 0.003) but the mean B–R is not significantly different (P = 0.226). Figure 8 strongly suggests that the MG survey is missing a significant number of LPVs with B–R color indices in the 1.5–4.5 range, perhaps for reasons discussed below.

Characterizing the Gaia DR2 LPVs by amplitude in period-color space shows a strong clustering of the higher amplitude

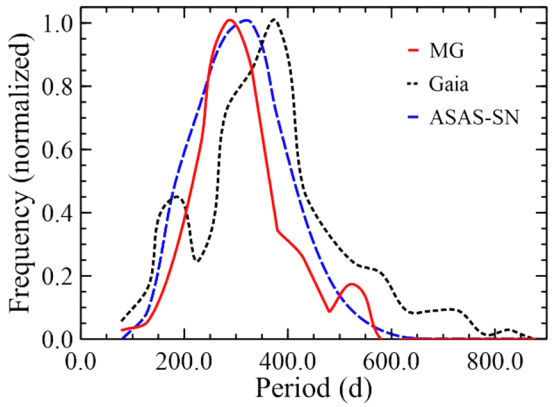


Figure 3. Distribution of observed periods in sky surveys.

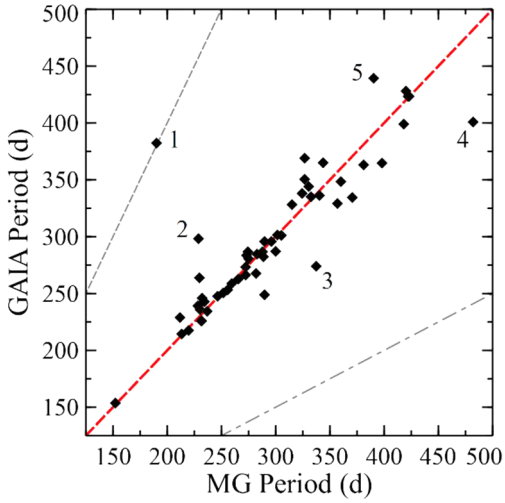


Figure 4. Comparison of determined periods for screened objects with those from GaiaDR2 survey (Mowlavi 2018). The labeled outliers are (1) MG6A 10639637, (2) MG6A 10722590, (3) MG6A 10637601, (4) MG1A 10696051, and (5) MG6A 10644124. Gray dashed line is second harmonic for MG period and gray dot-dash line is second harmonic for Gaia period.

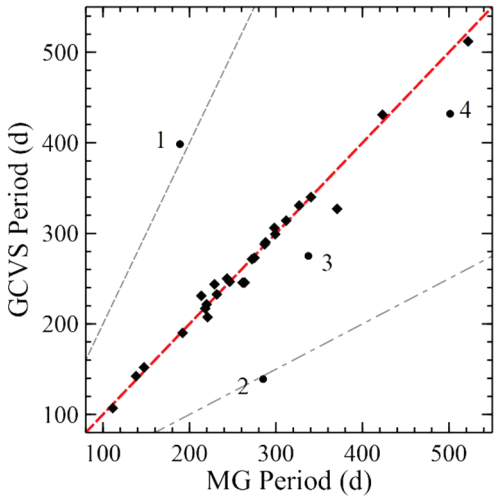


Figure 5. Correlation of MG periods with published GSVS periods. The labeled outlier objects are (1) MG1-1388633, (2) MG6A 10854654, (3) MG6A 10637601, and (4) MG1A 10624436. Gray dashed line is second harmonic for MG period and gray dot-dash line is second harmonic for Gaia period.

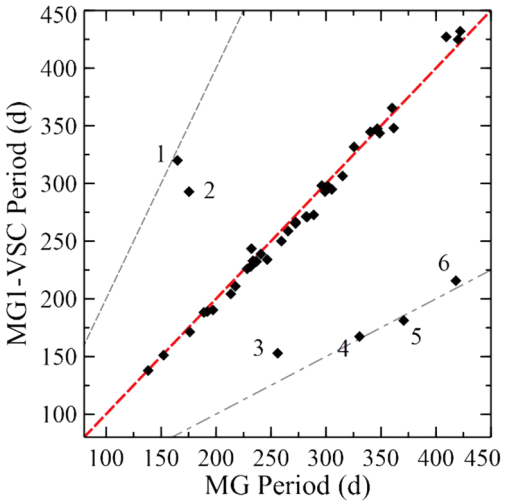


Figure 6. Correlation of originally reported periods with those determined using combined data from MG1 and MG6 surveys. The labeled outliers are (1) MG1-1376419, (2) MG6A 10660631, (3) MG6A 10620863, (4) MG1-1468465, (5) MG6A 10566412, and (6) MG1A 10658602. Gray dashed line is second harmonic for MG period and gray dot-dash line is second harmonic for MG1-VSC period.

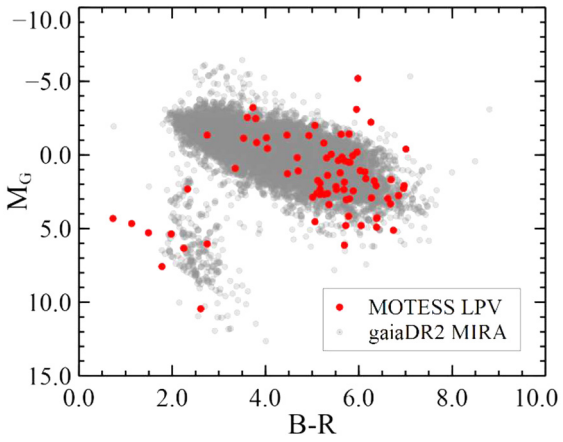


Figure 7. Color magnitude diagram (MG, is the absolute Gaia G magnitude; B–R, is the Gaia B minus R band color index). All color data are from the Gaia database (Gaia Collab., *et al.* 2018).

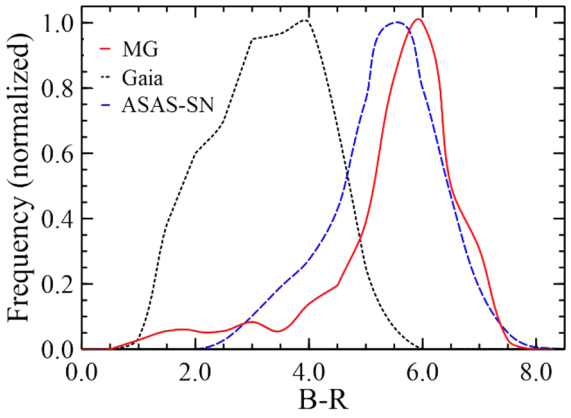


Figure 8. Comparison of redness distribution of MG objects with Gaia DR2 and ASAS-SN survey objects. All color data are from the Gaia database (Gaia Collab. *et al.* 2018).

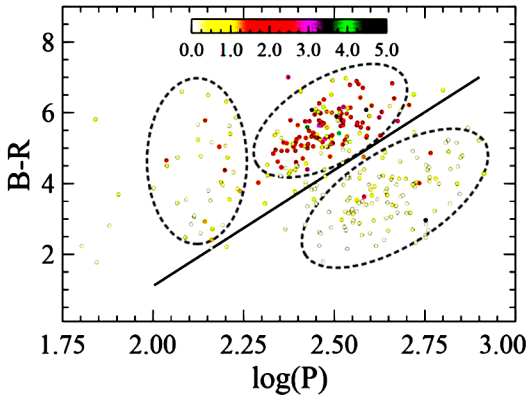


Figure 9. Period color diagram for the Gaia DR2 LPV in the MG1 survey strip. The color map indicates the amplitude of the object. Three visual clusters are demarcated by the dashed gray line. The line is drawn to separate the two main clusters in color, period space.

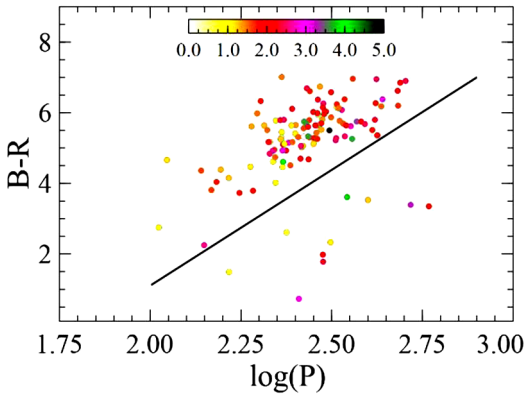


Figure 10. Period color diagram for the MOTESS LPV in the MG1 survey strip. The B–R color index is plotted as a function of the log of the period. The color map indicates the amplitude of the object. The line separating period, color space is from Equation (5).

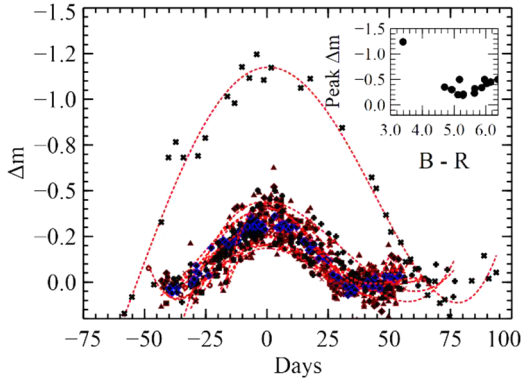


Figure 11. Humps (change in magnitude, Δm, of detrended light curve segment) from 15 LPVs with the peaks centered at 0 days. The inset shows the Δm at the peak value for each LPV as a function of color (the B–R bandpasses from Gaia measurements).

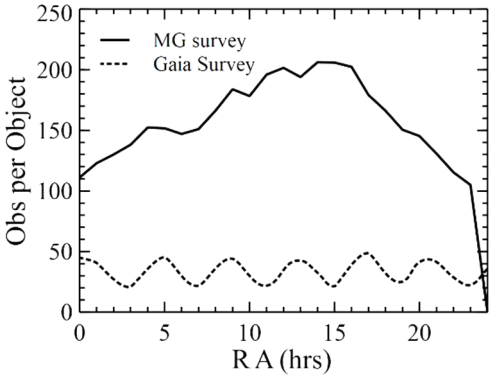


Figure 12. Mean number of observations per object as a function of RA for the MG and Gaia surveys.

Table 2. Comparison of object mean amplitudes(A) in magnitude and frequency (%) above and below the period color line (PCL) from Figure 9 between MG and Gaia DR2 surveys.

| | *Above PCL* | | *Below PCL* | | |
|---|---|---|---|---|---|
| *Source* | *%* | *A* | *%* | *A* | *P*† |
| MG | 80.6 | 2.03 | 19.4 | 2.15 | 0.71 |
| Gaia DR2 | 61.2 | 1.31 | 38.8 | 0.36 | $<10^{-5}$ |
| P | | $<10^{-4}$ | | $<10^{-4}$ | |

†*P, probability amplitudes are the same by student t-test.*

Table 3. MG LPVs that exhibit "Humps."

| *Source* | *Identifier* | *Δm* | *Days* | *Phase* |
|---|---|---|---|---|
| †MG6A | 10282350 | –0.45 | 51 | 0.80 |
| *MG1 | 1098444 | –0.35 | 47 | 0.73 |
| MG6A | 10624347 | –0.21 | 45 | 0.71 |
| †MG6A | 10634536 | –0.50 | 69 | 0.62 |
| MG6A | 10641834 | –0.32 | 55 | 0.70 |
| †MG6A | 10654089 | –0.50 | 61 | 0.74 |
| *MG1 | 1334111 | –0.42 | 50 | 0.79 |
| *MG1 | 1339600 | –0.19 | 45 | 0.78 |
| *MG1 | 1341934 | –0.30 | 34 | 0.70 |
| †MG6A | 10680158 | –0.20 | 49 | 0.65 |
| †MG1A | 10619638 | –1.24 | 107 | 0.71 |
| †MG6A | 10731840 | –0.50 | 65 | 0.75 |
| MG1A | 10647664 | –0.23 | 55 | 0.74 |
| *†MG1 | 1414532 | –0.34 | 64 | 0.71 |
| †MG6A | 10767909 | –0.30 | 46 | 0.79 |

**Previously noted (Craine* et al. *2015).* †*LPVs with humps in multiple cycles.*

objects in a redder region compared to the low amplitude objects. A period color line (PCL) can be drawn to separate the two main clusters shown in Figure 9 defined as:

$$B–R = 6.55 \log P – 12.0, \quad (5)$$

where P is the period in days and B–R is the color index. There is a third apparent cluster of low period objects that also tend to have low amplitude but on the redder side of the line.

Characterizing the MG survey LPVs in a similar manner, as shown in Figure 10, reveals that the low amplitude bluer cluster is only about half as abundant (19.4% of objects) compared to the Gaia DR2 survey (38.8% of objects), Table 2. The small number of objects in the region of the bluer cluster are mostly high amplitude and not different from the redder cluster (2.15 compared to 2.03, $P_{same} = 0.71$). The MG survey objects in the bluer cluster, however, do have a significantly higher amplitude than those from the Gaia DR2 survey (2.15 compared to 0.36, $P_{same} = 4.2 \times 10^{-5}$). The redder cluster has the characteristics of typical MIRA Mira type stars while the bluer cluster may represent the abundant Optical Gravitational Lensing Experiment (OGLE) Small Amplitude Red Giants (OSARGs) (Gaia Collab. *et al.* 2019).

3.2.3. LPVs with humps

The LPVs identified by screening the MG1 and MG6 surveys were examined to determine which might exhibit recognizable "hump" structures. The humps were best recognized in the Zwicky Transient Facility light curves of the identified LPVs (Bellm *et al.* 2019). Humps were found in 15 of the sample LPVs (see Table 3). Eight of the LPVs were observed to have humps in multiple cycles and are identified in Table 3 with a dagger. The best delineated hump from each of the LPVs was selected for further characterization. The region of the light curve with the hump was analyzed by fitting a high order polynomial to the points surrounding the hump to establish a baseline for detrending the data (see section 2.6 for details). The detrended data can be seen in the graphs in Appendix C. The maximum difference of the hump from the baseline is presented in the Table 3 as Δm (change in magnitude in the R band). The duration of the hump is reported as "days." The phase at which the hump peak occurred is listed as "phase" in the table. The asterisk denotes an LPV that was noted to have a hump in the original MG1 study (Craine *et al.*, 2015).

To facilitate the comparison of the population of humps they are plotted together in Figure 11, with the hump peaks normalized to day 0. Most of the humps are very similar in shape and magnitudes. However, the hump observed for MG1A 1785161 was noticeably brighter in magnitude (Δm = –1.24 versus an average of –0.40) and duration (107 d versus an average of 56.2 d). It is intriguing that this LPV was the least red of the group (B–R = 3.39 versus and average of 5.37).

## 4. Discussion

The new reduction of the MG1 and MG6 surveys has resulted in the expanded identification of LPV stars in the MG1 strip with approximated R magnitudes between ~12.6 and ~17.4 from the initial 47 (Kraus, *et al.* 2007) to the current 138. Review of the compilation catalogs of the GCVS (Samus *et al.* 2017) and AAVSO (International Variable Star Index; VSX), in addition to the large collection of automated identification of LPV candidates from the Gaia survey (Gaia Collab. *et al.* 2018, 2019) and the ASAS-SN survey (Kochanek *et al.* 2017; Shappee *et al.* 2014), revealed that this study has newly identified nine unique LPVs (marked with an asterisk in Appendix A Tables A1 and A2). This brings the total number of new LPV identifications from the MOTESS-GNAT survey to 56 (including those reported in (Kraus *et al.* 2007)).

The surveys referenced in this study each have unique characteristics which are based upon the observing strategy, equipment, and whether ground-based, or space-based. These characteristics manifest themselves in the number of observations per object and the cadence of these observations, which in turn impacts the ability to define a period. For example, comparing the MG survey with the Gaia survey shows that the MG survey has accumulated a greater number of observations per object and that the number of observations per object is a function of the RA, with the most productive period around 14 to 15 hours. The pattern of observation for the space-based Gaia satellite however is quite different (see Figure 12).

The number of observations obtained by the MG survey is an advantage although it may be offset by seasonal gaps in observing. The Gaia survey observes objects more regularly, which more closely satisfies some of the basic assumptions of key frequency analysis methods. In addition, the Gaia survey has superior precision, with typical normalized errors of about 0.1%, compared to the MG errors of about 1%. The result is, as shown in Figure 4, the general agreement in period determinations. However, there are several objects where even the Gaia data benefits from the complementary data from ground-based surveys.

The MG survey collects unfiltered imaging. The impact on color properties of identified LPVs can be observed in Figures 8–10. These results revealed a bias in color of identified LPVs from the MG survey compared to those reported for the Gaia survey (Gaia Collab. *et al.* 2019). First, this bias is due to the bluer population of stars included in the Gaia LPVs (e.g., OSARGs) being fainter in the red magnitude. This results in a decreased signal signal-to to-noise ratio, increasing the variance in the MG survey photometry (which is already greater than that of the Gaia survey) and contributing to underrepresentation of some Gaia objects in the MG survey. Second, the bluer Gaia population of LPVs displays smaller amplitudes than the redder MIRA type stars, limiting their survival of the screening method employed (i.e., μ and 1/η).

The differences in the various surveys provide a strong argument for using the data in a complementary fashion to compensate for the shortcomings of each survey. Notable among surveys areis the data produced by the Zwicky Transient Facility (Bellm *et al.* 2019) that combines precision and large sample sizes which can be highly synergistic. The current trend of providing the ability to cross-reference the different surveys (such as at the Vizier (https://vizier.u-strasbg.fr/viz-bin/VizieR) or Gaia (https://gea.esac.esa.int/archive/) web portals) is important for both the amateur and professional astronomer and needs to be expanded.

**5. Acknowledgements**

This research has made use of the International Variable Star Index (VSX) database, operated at AAVSO, Cambridge, Massachusetts, USA.

**References**

Astropy Collaboration. 2018, *Astron. J.*, **156**, 123.

Baluev, R. V. 2012, *Mon. Not. Roy. Astron. Soc.*, **422**, 2372.

Bellm E. C., *et al*. 2019, *Publ. Astron. Soc. Pacific*, **131**, 18002.

Bradley, L., *et al.* 2019, astropy/photutils: v0.6 (https://doi.org/10.5281/ZENODO.2533376).

Craine, B. L., Craine, E. R., Tucker, T. A., Culver, R. B., and Anderson, R. 2021, in *Proceedings for the 40th Annual Symposium of the Society for Astronomical Sciences SAS-2021*, eds. J. C. Martin, R. K. Buchheim, R. M. Gill, W. Green, R. Stephens, Society for Astronomical Sciences, Rancho Cucamonga, CA, 31.

Craine, E. R., Culver, R. B., Eykholt, R., Flurchick, K. M., Kraus, A. L., Tucker, R. A., and Walker, D. K. 2015, *J. Amer. Assoc. Var. Star Obs.*, **43**, 131.

Craine, E. R., Culver, R. B., Kraus, A. L., Tucker, R. A., Walker, D., and Wing, R. F. 2007, in *The Society for Astronomical Sciences 26th Annual Symposium on Telescope Science*, Society for Astronomical Sciences, Rancho Cucamonga, CA, 45.

Gaia Collaboration, Brown, A. G. A., *et al.* 2018, *Astron. Astrophys.*, **616A**, 1.

Gaia Collaboration, Eyer, L., *et al.* 2019, *Astron. Astrophys.*, **623A**, 110.

Kochanek, C. S., *et al.* 2017, *Publ. Astron. Soc. Pacific*, **129**, 104502.

Kraus, A. L., Tucker, R. A., Thompson, M. I., Craine, E. R., and Hillenbrand, L. A. 2011, *Astrophys. J.*, **728**, 48.

Kraus, Adam L., Craine, Eric R., Giampapa, Mark S., Scharlach, W. W. G., and Tucker, Roy A. 2007, *Astron. J.*, **134**, 1488.

Mowlavi, N. 2018, *Astron. Astrophys.*, **618A**, 58.

Percy, J. R. 2007, *Understanding Variable Sstars*, Cambridge Univ. Press., Cambridge, 209.

Press, W. H., Teukolsky, S. A., Vetterling, W. T., and Flannery, B. P. 1996, *Numerical Recipes in Fortran 90*, Cambridge Univ. Press, Cambridge.

Samus, N. N., Kazarovets, E. V., Durlevich, O. V., Kireeva, N. N., and Pastukhova, E. N. 2017, *Astron. Rep.*, **61**, 80.

Scargle, J. D. 1982, *Astrophys. J.*, **263**, 835.

Shappee, B. J., *et al.* 2014, *Astrophys. J.*, **788**, 48.

Tucker, R. A. 2007, *Astron. J.*, **134**, 1483.

VanderPlas, J. T. 2018, *Astrophys. J., Suppl. Ser.*, **236**, 16.

Virtanen, P., *et al.* 2020, *Nat. Methods*, **17**, 261.

Von Neumann, J. 1941, *Ann. Math. Statistics*, **12**, 367.

Welch, D. L., and Stetson, P. B. 1993, *Astron. J.*, **105**, 1813.

Zechmeister, M. 2019, "GLS/Python at Master-Mzechmeister/GLS," (github.com/mzechmeister/GLS/tree/master/python) accessed 12 Dec. 2022.

Zechmeister, M., and Kürster, M. 2009, *Astron. Astrophys.*, **496**, 577.

**Appendix A: Tables of LPV**

*Table A1. Long period variable stars with high confidence periods. Objects identified as new LPVs in this study are marked with an asterisk.*

| Database ID | | | | | | | | |
|---|---|---|---|---|---|---|---|---|
| *MG1-VSC* | *MG1A* | *MG6A* | *R.A. (2000) h* | *Dec. (2000) °* | *mMG*[1] | *Amplitude (mag)* | *Period (d)* | *Epoch*[2] *(MJD)* |
| — | — | 10125719 | 6.27973 | 3.48849 | 12.74 | 1.56 | 333 | 52018.7 |
| — | — | 10157151 | 6.66172 | 3.41147 | 12.55 | 2.47 | 344 | 52200.1 |
| — | — | 10245630 | 7.39174 | 3.16072 | 13.02 | 0.98 | 106 | 52224.6 |
| — | — | 10282350 | 7.86004 | 3.48481 | 11.87 | 1.05 | 327 | 51923.4 |
| — | — | 10313628 | 8.58345 | 2.99139 | 12.99 | 2.91 | 257 | 52219.8 |
| — | — | 10318510 | 8.75614 | 3.45367 | 13.67 | 1.24 | 398 | 52208.8 |
| — | 10412126 | — | 17.44638 | 3.46843 | 11.44 | 1.38 | 261 | 51899.2 |
| — | 10420454 | 10492206 | 17.56957 | 3.05137 | 11.84 | 0.90 | 218 | 52023.6 |
| — | 10424503 | 10496867 | 17.62531 | 3.45457 | 12.51 | 1.71 | 275 | 52356.4 |
| — | — | 10514819 | 17.83027 | 3.28816 | 11.99 | 1.70 | 220 | 51852.9 |
| — | — | 10525998 | 17.92806 | 3.03218 | 12.98 | 2.26 | 416 | 51968.1 |
| — | — | 10538157 | 18.01871 | 3.55115 | 12.61 | 1.65 | 147 | 52041.0 |
| 1098444 | — | 10541529 | 18.04222 | 3.08712 | 14.30 | 2.12 | 259 | 51805.2 |
| 1117392 | — | 10549004 | 18.08990 | 2.94400 | 13.00 | 1.97 | 192 | 51898.2 |
| 1155788 | — | 10566412 | 18.17950 | 2.95202 | 14.29 | 3.35 | 371 | 51827.2 |
| — | — | 10577762 | 18.24071 | 3.10995 | 12.44 | 1.30 | 156 | 51987.2 |
| — | — | 10589271 | 18.29673 | 3.66614 | 12.20 | 1.60 | 243 | 51991.4 |
| — | — | 10595142 | 18.32747 | 3.21517 | 13.26 | 1.66 | 274 | 51858.8 |
| — | — | 10596880 | 18.33669 | 3.54930 | 14.14 | 2.04 | 273 | 51943.6 |
| — | — | 10597482 | 18.33939 | 3.43108 | 12.59 | 0.97 | 221 | 52036.2 |
| 1248064 | 10521961 | 10608672 | 18.39271 | 3.41298 | 13.77 | 1.83 | 283 | 51830.3 |
| — | — | 10610820 | 18.40066 | 3.18591 | 13.31 | 1.53 | 210 | 51966.4 |
| 1258871 | — | 10614674 | 18.42071 | 3.67411 | 13.33 | 1.87 | 232 | 51815.5 |
| — | — | 10615458 | 18.42484 | 3.04575 | 14.30 | 1.03 | 230 | 51875.6 |
| — | 10528529 | 10616558 | 18.43054 | 3.21746 | 11.78 | 1.21 | 264 | 51891.3 |
| 1270097 | — | — | 18.44853 | 2.91056 | 13.70 | 2.42 | 234 | 52068.7 |
| 1270289 | — | 10620863 | 18.44899 | 3.22180 | 13.70 | 1.84 | 265 | 51938.1 |
| — | — | 10623473 | 18.45900 | 3.23070 | 13.87 | 1.25 | 165 | 52001.4 |
| — | — | 10624347 | 18.46358 | 3.17335 | 12.63 | 0.72 | 230 | 51915.6 |
| 1287551 | — | — | 18.49306 | 3.47056 | 13.53 | 2.45 | 420 | 51821.8 |
| 1291327 | — | — | 18.50289 | 3.39167 | 13.40 | 2.84 | 241 | 51855.4 |
| — | — | 10634536 | 18.51324 | 3.68385 | 13.88 | 1.25 | 214 | 52004.8 |
| — | — | 10637601 | 18.53199 | 3.03832 | 13.13 | 2.58 | 337 | 51903.6 |
| — | — | 10638266 | 18.53610 | 3.54179 | 14.25 | 2.51 | 300 | 52010.2 |
| — | — | 10638788 | 18.53956 | 3.68264 | 14.21 | 2.10 | 212 | 51842.1 |
| — | — | 10639637 | 18.54536 | 3.59500 | 14.66 | 1.35 | 190 | 52009.6 |
| — | 10549295 | — | 18.55313 | 2.91184 | 13.25 | 1.63 | 265 | 52000.8 |
| — | — | 10641834 | 18.56043 | 3.34669 | 13.00 | 1.40 | 252 | 51809.1 |
| — | — | 10643445 | 18.57031 | 3.41909 | 14.25 | 2.47 | 456 | 52082.5 |
| — | — | 10644124 | 18.57412 | 3.00430 | 14.33 | 2.45 | 390 | 52034.0 |
| — | — | 10646120 | 18.58583 | 3.39812 | 14.52 | 0.78 | 237 | 51885.4 |
| 1315064 | 10554843 | 10646737 | 18.58913 | 3.64086 | 14.56 | 2.00 | 299 | 51801.2 |
| — | — | 10650043* | 18.60816 | 3.62960 | 13.59 | 2.08 | 481 | 51917.2 |
| 1326286 | — | 10654089 | 18.62912 | 3.65812 | 15.21 | 1.82 | 302 | 52020.4 |
| — | — | 10656955 | 18.64352 | 3.12275 | 12.93 | 2.18 | 381 | 51947.3 |
| — | — | 10658268 | 18.65026 | 3.57515 | 14.15 | 1.77 | 327 | 52044.1 |
| — | — | 10658466 | 18.65129 | 3.69543 | 14.66 | 2.49 | 324 | 51896.1 |
| 1334111 | — | 10659344 | 18.65542 | 3.05212 | 14.71 | 1.96 | 305 | 52040.0 |

*Table continued on following pages*

*Table A1. Long period variable stars with high confidence periods (cont.).*

| Database ID | | | | | | | | |
|---|---|---|---|---|---|---|---|---|
| *MG1-VSC* | *MG1A* | *MG6A* | *R.A. (2000) h* | *Dec. (2000) °* | *mMG*[1] | *Amplitude (mag)* | *Period (d)* | *Epoch*[2] *(MJD)* |
| — | 10566760 | 10659797 | 18.65731 | 3.28148 | 13.59 | 2.24 | 290 | 51772.5 |
| 1336304 | — | — | 18.66331 | 3.08861 | 13.96 | 1.70 | 362 | 51971.4 |
| — | — | 10663230 | 18.67001 | 3.64038 | 14.42 | 1.32 | 296 | 51866.2 |
| — | — | 10664502 | 18.67500 | 3.60400 | 12.81 | 1.09 | 251 | 51979.6 |
| 1339600 | — | 10664704 | 18.67601 | 3.42910 | 14.89 | 2.44 | 325 | 51902.2 |
| 1341934 | 10572125 | 10666775 | 18.68734 | 3.33558 | 14.77 | 2.18 | 237 | 52032.8 |
| — | — | 10666916 | 18.68815 | 3.47474 | 13.87 | 1.13 | 245 | 51912.8 |
| — | 10573832 | — | 18.69702 | 2.91197 | 15.37 | 2.74 | 357 | 51808.8 |
| 1344747 | 10574581 | — | 18.70092 | 3.09939 | 14.79 | 1.51 | 197 | 51863.4 |
| — | 10575668 | 10670584 | 18.70721 | 2.96925 | 15.43 | 2.59 | 141 | 52037.8 |
| — | — | 10671162 | 18.71028 | 3.65455 | 15.55 | 4.09 | 232 | 51931.4 |
| — | 10581264 | 10676905 | 18.74174 | 3.36799 | 15.38 | 0.58 | 292 | 51820.2 |
| — | 10583328 | — | 18.76376 | 2.97547 | 15.74 | 1.29 | 206 | 52023.8 |
| — | — | 10679837* | 18.77205 | 3.47107 | 15.43 | 1.94 | 303 | 51822.6 |
| — | 10583952 | — | 18.77278 | 2.99682 | 14.77 | 2.08 | 315 | 51843.3 |
| — | — | 10679937 | 18.77355 | 3.56562 | 13.41 | 0.88 | 234 | 51854.0 |
| — | — | 10680158 | 18.77661 | 3.62856 | 15.84 | 1.59 | 205 | 51920.1 |
| — | — | 10680181* | 18.77706 | 3.24949 | 15.81 | 1.35 | 218 | 51981.6 |
| — | — | 10681094 | 18.79188 | 2.94482 | 16.36 | 1.87 | 202 | 51877.4 |
| — | 10585083 | 10681185 | 18.79312 | 3.31842 | 15.06 | 1.77 | 275 | 52003.7 |
| — | — | 10682562 | 18.81648 | 3.41414 | 15.28 | 1.77 | 343 | 51891.9 |
| — | 10586841 | 10683307 | 18.82688 | 3.02730 | 16.22 | 2.47 | 260 | 51793.1 |
| — | — | 10683894* | 18.83644 | 3.48245 | 15.25 | 2.40 | 506 | 51956.7 |
| — | 10589889* | — | 18.88252 | 3.03746 | 14.95 | 1.94 | 586 | 51903.5 |
| — | 10592725 | 10690206 | 18.93340 | 2.99415 | 11.79 | 1.48 | 230 | 51828.9 |
| — | 10593262* | 10690831* | 18.94750 | 2.91795 | 13.21 | 2.32 | 270 | 52024.9 |
| — | — | 10691652 | 18.96674 | 3.47641 | 15.78 | 1.54 | 433 | 51727.2 |
| — | 10595225 | — | 18.98945 | 3.11190 | 15.67 | 1.36 | 294 | 51954.8 |
| — | — | 10699251 | 19.04595 | 3.44845 | 12.77 | 2.07 | 489 | 52067.5 |
| — | — | 10703054* | 19.05968 | 3.46663 | 15.50 | 3.62 | 269 | 51834.5 |
| 1372707 | — | — | 19.07372 | 3.42139 | 15.51 | 4.17 | 349 | 52222.6 |
| — | — | 10707886 | 19.07564 | 3.36433 | 14.87 | 1.07 | 222 | 51831.0 |
| 1376419 | — | — | 19.08364 | 3.17194 | 15.22 | 0.80 | 165 | 51910.6 |
| 1379672 | — | 10713590 | 19.09167 | 3.55671 | 13.75 | 1.83 | 152 | 52041.5 |
| — | 10619638 | — | 19.09897 | 2.94856 | 14.01 | 3.24 | 522 | 51528.3 |
| — | — | 10717332 | 19.09977 | 3.57870 | 13.39 | 1.10 | 290 | 51893.5 |
| — | 10623199 | — | 19.10785 | 3.17282 | 13.73 | 1.54 | 221 | 51831.3 |
| — | 10624436 | — | 19.11093 | 3.44052 | 13.19 | 3.25 | 501 | 51979.7 |
| 1388413 | — | 10721993 | 19.11139 | 3.03939 | 13.34 | 1.57 | 246 | 51824.1 |
| 1388633 | — | — | 19.11197 | 3.28667 | 13.65 | 1.12 | 189 | 52035.4 |
| — | 10625131 | 10722447 | 19.11257 | 3.27738 | 13.77 | 4.97 | 312 | 51748.3 |
| — | — | 10722590 | 19.11300 | 3.42302 | 12.40 | 1.22 | 229 | 51890.8 |
| — | 10626627 | — | 19.11614 | 2.98712 | 14.32 | 2.12 | 423 | 51831.7 |
| 1391053 | — | — | 19.11625 | 2.98722 | 14.11 | 1.91 | 422 | 51838.6 |
| — | — | 10725247 | 19.12023 | 3.35178 | 13.09 | 1.36 | 298 | 51752.6 |
| 1393846 | — | — | 19.12111 | 2.95944 | 13.67 | 3.71 | 360 | 51739.5 |
| — | 10634557 | — | 19.13294 | 3.30466 | 15.28 | 2.08 | 246 | 51997.1 |
| — | — | 10731840 | 19.14089 | 3.26123 | 15.21 | 3.10 | 437 | 51777.9 |

*Table continued on next page*

*Table A1. Long period variable stars with high confidence periods (cont.).*

| Database ID | | | | | | | | |
|---|---|---|---|---|---|---|---|---|
| *MG1-VSC* | *MG1A* | *MG6A* | *R.A. (2000) h* | *Dec. (2000) °* | *mMG*[1] | *Amplitude (mag)* | *Period (d)* | *Epoch*[2] *(MJD)* |
| 1406788 | 10642204 | — | 19.15478 | 2.91548 | 13.31 | 2.07 | 299 | 51757.6 |
| 1410977 | — | — | 19.16472 | 2.90583 | 13.40 | 1.61 | 340 | 52001.4 |
| 1413873 | 10647664 | 10742975 | 19.17113 | 3.03156 | 15.13 | 2.09 | 347 | 52012.4 |
| 1414532 | — | — | 19.17256 | 2.96806 | 13.39 | 1.59 | 315 | 51849.6 |
| 1428501 | 10658602 | — | 19.20193 | 3.05442 | 13.29 | 1.92 | 418 | 51714.5 |
| — | — | 10759858 | 19.22240 | 3.30691 | 13.17 | 1.09 | 314 | 51946.7 |
| 1440964 | — | — | 19.23317 | 3.12889 | 13.70 | 1.88 | 409 | 51918.1 |
| 1444065 | 10670343 | 10764936 | 19.24078 | 3.18946 | 13.46 | 3.66 | 266 | 51908.1 |
| — | — | 10765454 | 19.24268 | 3.21684 | 12.72 | 2.08 | 281 | 51896.5 |
| 1448319 | 10673873 | 10767909 | 19.25080 | 2.91731 | 13.43 | 2.67 | 218 | 51929.0 |
| 1457857 | — | — | 19.27147 | 3.61722 | 13.07 | 1.16 | 282 | 51896.1 |
| — | — | 10776316 | 19.27731 | 3.42775 | 12.58 | 1.77 | 289 | 52008.5 |
| 1466778 | 10685409 | 10780200 | 19.29204 | 3.38649 | 14.25 | 2.00 | 296 | 51796.3 |
| 1468465 | — | — | 19.29603 | 2.92750 | 14.80 | 1.51 | 330 | 52007.2 |
| 1477416 | — | 10786863 | 19.31665 | 3.51341 | 13.35 | 1.63 | 138 | 52008.3 |
| — | 10696051 | — | 19.33167 | 3.37791 | 13.38 | 1.71 | 482 | 51713.4 |
| 1492532 | — | — | 19.35258 | 3.53500 | 14.14 | 2.49 | 213 | 51940.3 |
| 1496600 | 10704133 | 10798486 | 19.36387 | 3.51821 | 12.70 | 2.06 | 289 | 51843.2 |
| — | 10706234 | — | 19.37303 | 3.31331 | 12.60 | 1.55 | 288 | 51787.4 |
| — | — | 10805023 | 19.39115 | 3.32842 | 12.37 | 1.16 | 111 | 52005.2 |
| — | 10710722 | 10805298 | 19.39227 | 3.15070 | 11.99 | 1.56 | 256 | 51834.8 |
| 1518640 | — | — | 19.41364 | 3.62250 | 13.06 | 2.32 | 228 | 51944.0 |
| 1523972 | — | — | 19.42514 | 3.30889 | 13.86 | 2.21 | 272 | 52045.2 |
| 1540903 | — | — | 19.46025 | 3.38639 | 13.69 | 3.65 | 272 | 51902.5 |
| — | 10737124 | 10832301 | 19.49149 | 3.50998 | 13.79 | 2.28 | 300 | 51942.3 |
| — | — | 10854654 | 19.58874 | 3.65374 | 12.92 | 2.04 | 285 | 51775.7 |
| — | — | 10864634 | 19.63745 | 3.52213 | 12.37 | 1.94 | 214 | 52049.6 |
| — | 10777381 | — | 19.67851 | 3.20240 | 11.26 | 0.91 | 232 | 51918.7 |
| 1653368 | 10781632 | 10877309 | 19.70695 | 3.53429 | 13.02 | 3.08 | 232 | 51961.8 |
| — | — | 10897045 | 19.83316 | 3.15389 | 11.54 | 1.50 | 287 | 51848.8 |
| 1877036 | — | — | 20.47967 | 2.98500 | 14.15 | 1.87 | 176 | 51985.1 |

[1] *mMG, differential magnitude unfiltered.*
[2] *Epoch, establishes a zero-time at one period before the first maxima in the observed data.*

*Table A2. Long period variables with ambiguous periods. The period candidates have been evaluated by determining the Vuong statistic (Baluev 2012) and found to have p-values > 0.05 indicating that one of the periods could not be favored. Objects identified as new LPVs in this study are marked with an asterisk.*

| Database (ID) | | | | | | |
|---|---|---|---|---|---|---|
| *MG1-VSC* | *MG1A* | *MG6A* | *R.A. (2000) h* | *Dec. (2000) °* | *mMG*[1] | *Period (d)* |
| 1334664 | — | 10660631 | 18.66048 | 2.28784 | 14.10 | 119,175 |
| | | 10691329* | 18.95937 | 3.45862 | 15.39 | 199, 390 |
| — | 10595620* | — | 18.99722 | 3.64549 | 14.49 | 521, 456 |
| — | — | 10693742 | 19.00426 | 2.98192 | 14.69 | 598, 516 |
| 1375418 | — | — | 19.08108 | 2.90444 | 15.12 | 149, 540 |
| 165463 | 10629210 | — | 19.12164 | 2.99446 | 13.29 | 73,120 |
| — | 10632033 | 10727558 | 19.12709 | 3.49154 | 13.79 | 152, 146, 263 |
| 1410394 | — | — | 19.16333 | 3.57500 | 13.73 | 71, 88, 90, 121 |
| — | 10671116 | — | 19.24264 | 3.50580 | 14.92 | 526, 244 |
| 1478012 | — | — | 19.31811 | 3.40917 | 16.44 | 168, 338 |
| 1545107 | 10731356 | 10826002 | 19.46893 | 3.00822 | 14.37 | 170, 302 |

[1] *mMG, differential magnitude unfiltered.*

## Appendix B: Light curves for LPV stars

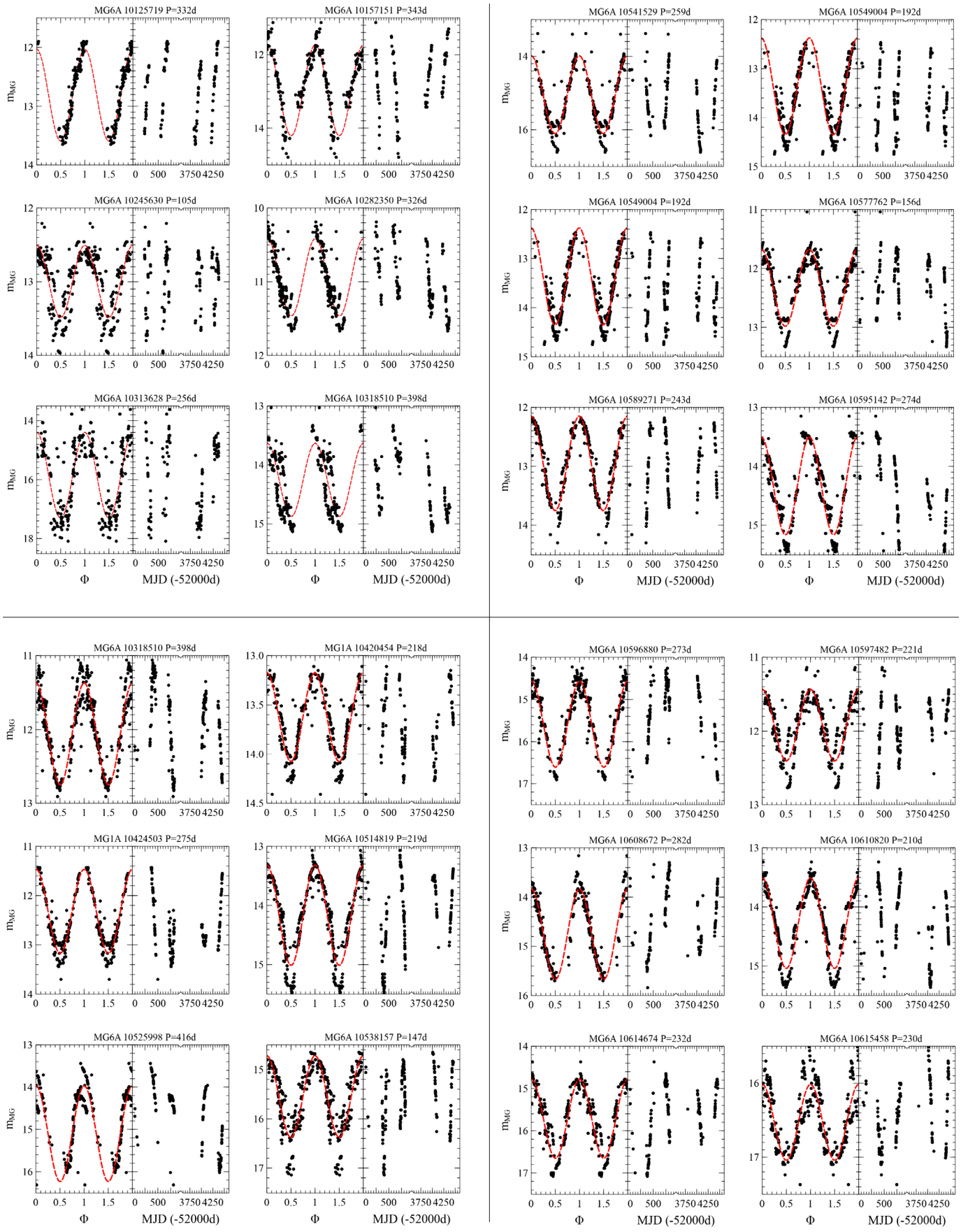


Figure B1. Light curves and folded phase light curves for LPVs with high confidence periods. Red dashed line is the least squares sinusoidal fit to the data. P is the period determined using the Lomb-Scargle GLS method. (Figure continued on following pages.)

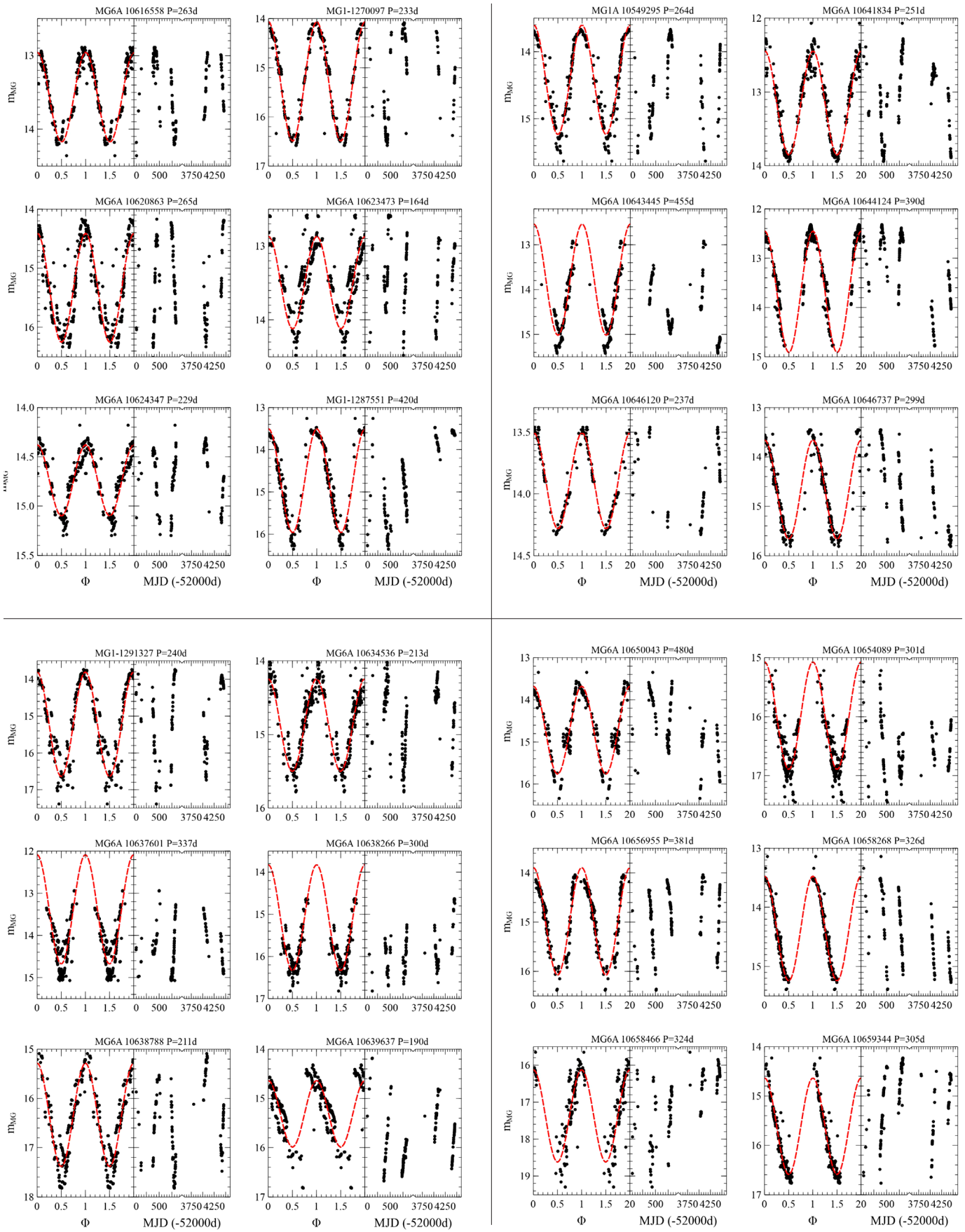


Figure B1. Light curves and folded phase light curves for LPVs with high confidence periods. Red dashed line is the least squares sinusoidal fit to the data. P is the period determined using the Lomb-Scargle GLS method (cont.). (Figure continued on following pages.)

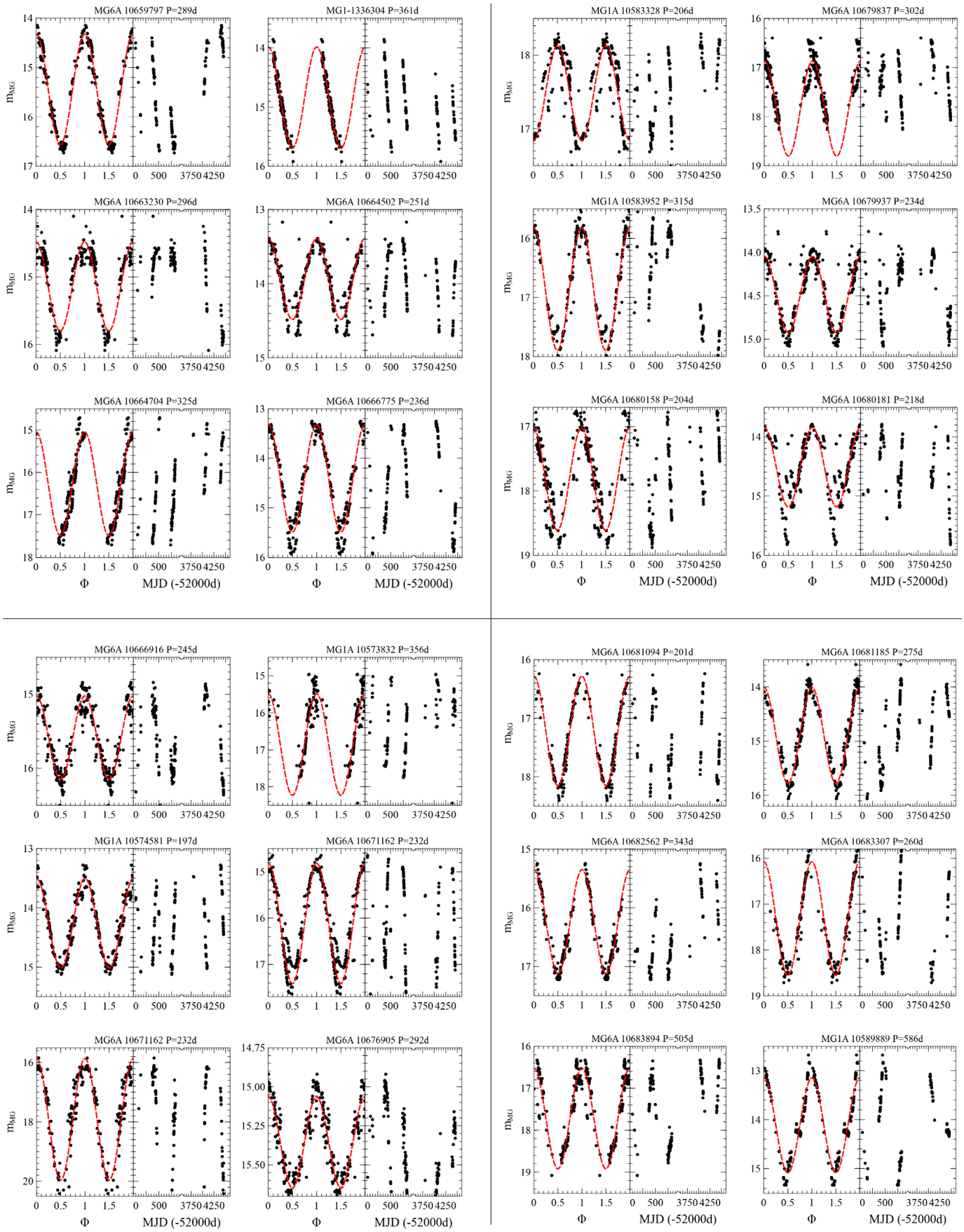


Figure B1. Light curves and folded phase light curves for LPVs with high confidence periods. Red dashed line is the least squares sinusoidal fit to the data. P is the period determined using the Lomb-Scargle GLS method (cont.). (Figure continued on following pages.)

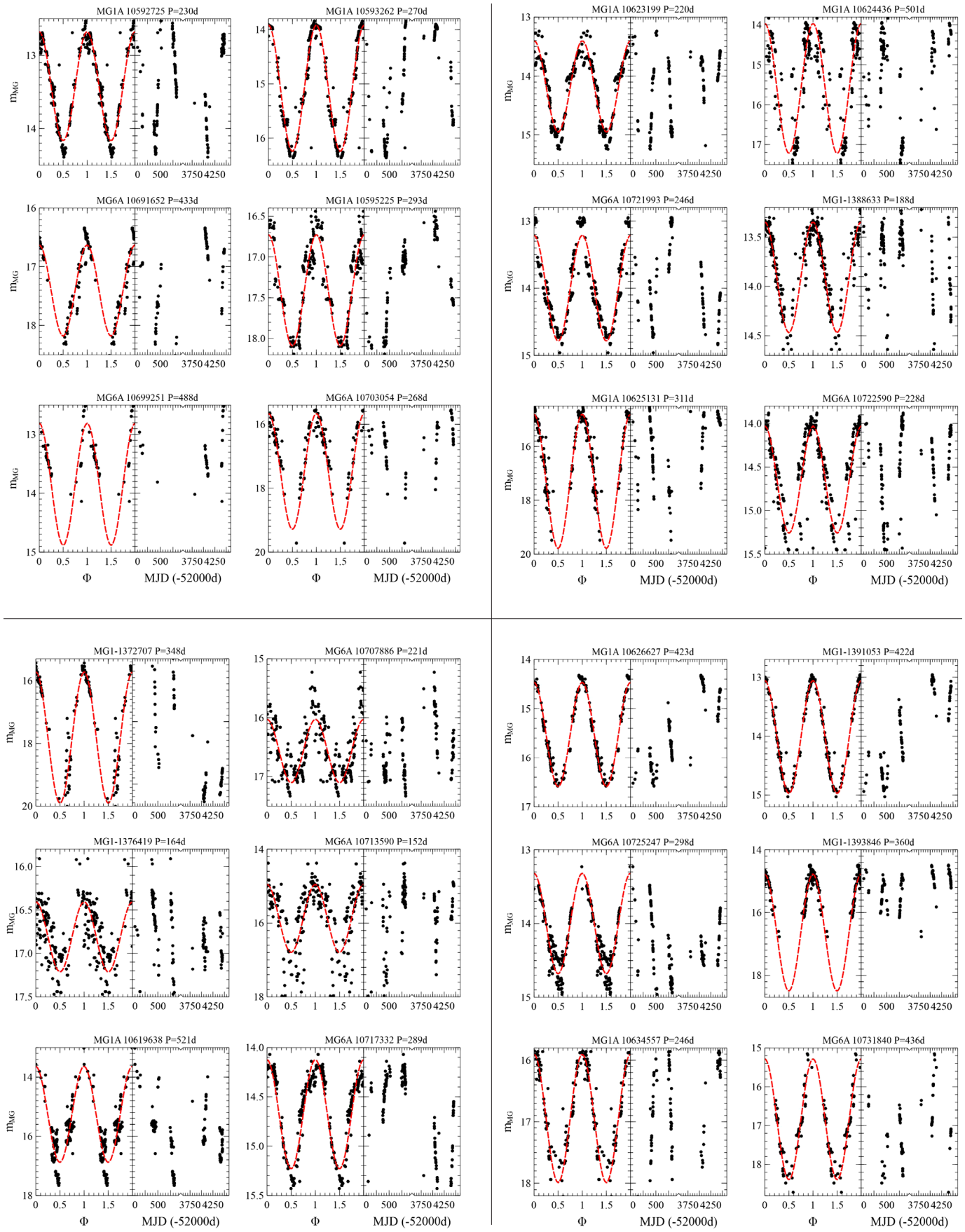


Figure B1. Light curves and folded phase light curves for LPVs with high confidence periods. Red dashed line is the least squares sinusoidal fit to the data. P is the period determined using the Lomb-Scargle GLS method (cont.). (Figure continued on following pages.)

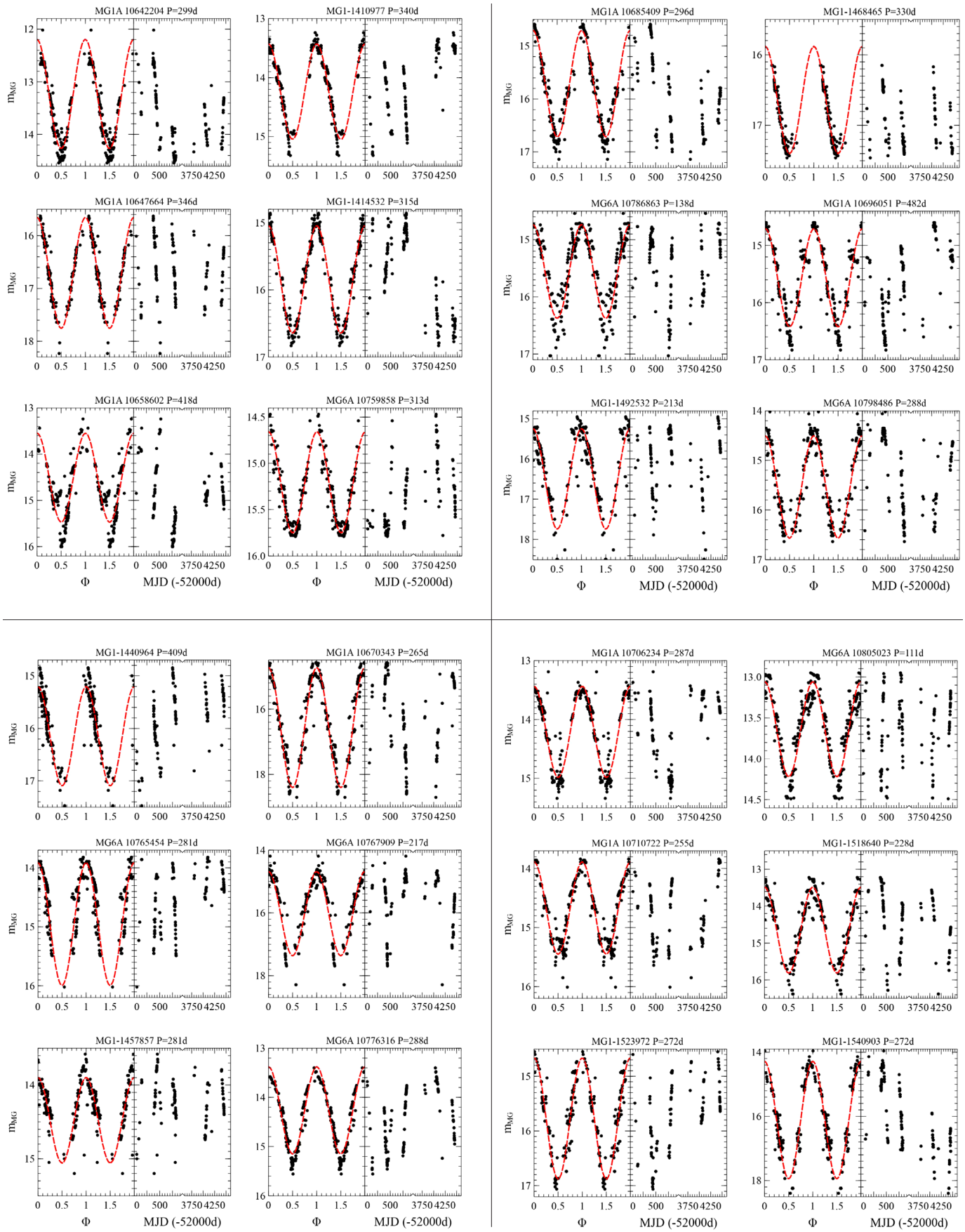


Figure B1. Light curves and folded phase light curves for LPVs with high confidence periods. Red dashed line is the least squares sinusoidal fit to the data. P is the period determined using the Lomb-Scargle GLS method (cont.). (Figure continued on next page.)

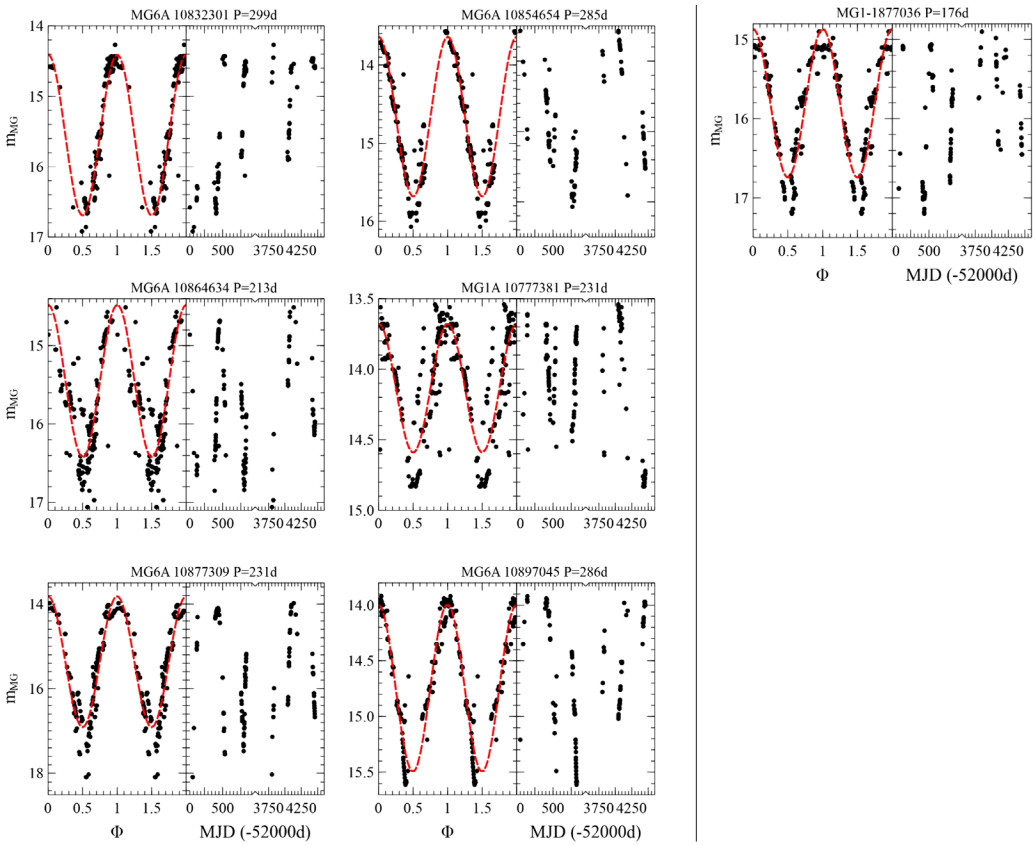


Figure B1. Light curves and folded phase light curves for LPVs with high confidence periods. Red dashed line is the least squares sinusoidal fit to the data. P is the period determined using the Lomb-Scargle GLS method (cont.).

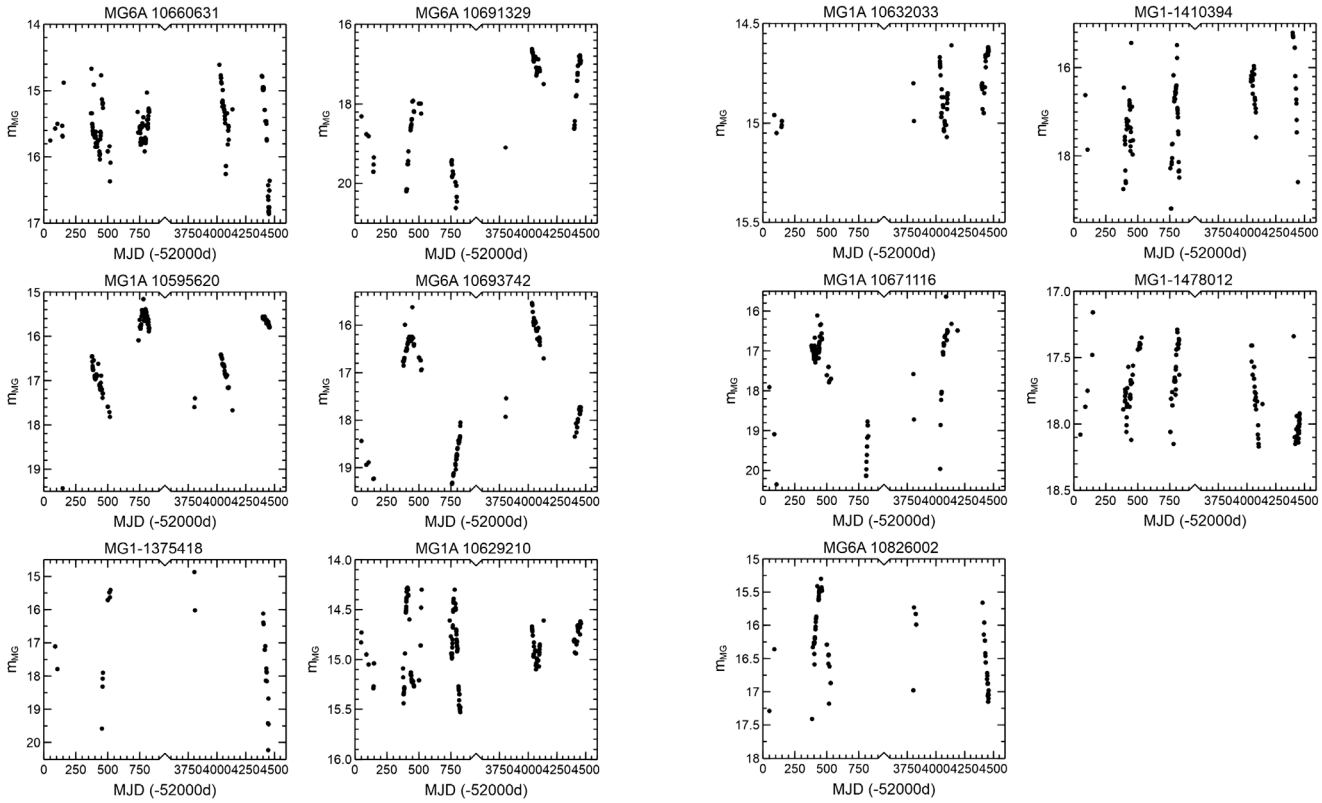


Figure B2. Light curves for LPVs with ambiguous periods. Data point before 52900 MJD are from the MG1 survey and those after 55750 MJD are from the MG6 survey.

## Appendix C: Light curves for hump feature

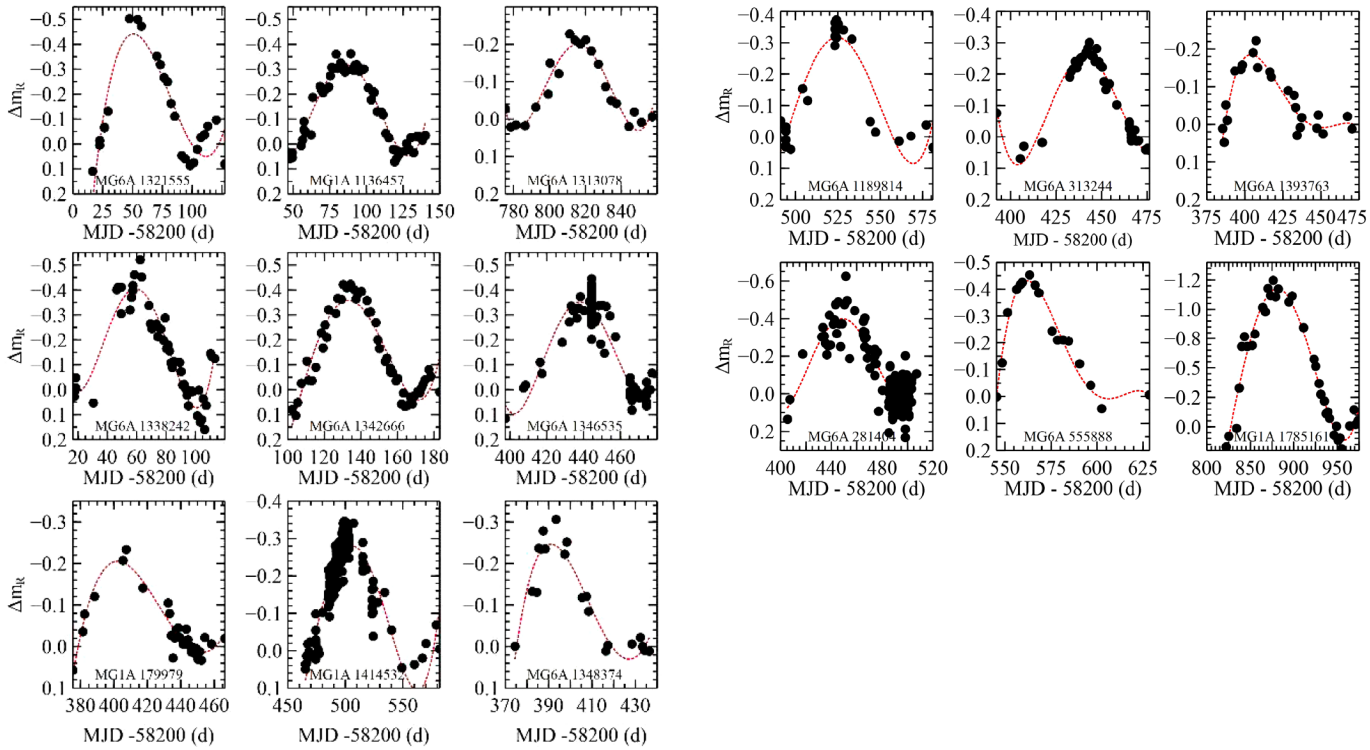


Figure C1. The region around the "hump" of an ascending or descending arm of the periodic light curves were detrended prior to plotting to facilitate the visualization of the hump. The data are from the ZTF survey R band (Bellm *et al.* 2019). The red dotted line is a fourth order polynomial fit to the hump.